Dynamics of polylactic acid under ultrafine nanoconfinement: the collective interface effect and the spatial gradient

Shiwang Cheng,^{1*} David Kogut,¹ Juncheng Zheng,¹ Shalin Patil,¹ Fuming Yang,² Weiyi Lu^{1,2}

Department of Chemical Engineering and Materials Science, Michigan State
 University, East Lansing, MI 48824, USA

 Department of Civil and Environmental Engineering, Michigan State University, East Lansing, MI 48824, USA

Abstract

Polymers under nanoconfinement can exhibit large alterations in dynamics from their bulk values due to an interface effect. However, understanding the interface effect remains a challenge, especially in the ultrafine nanoconfinement region. In this work, we prepare new geometries with ultrafine nanoconfinement $\sim 10~nm$ through controlled distributions of the crystalline phases and the amorphous phases of a model semi-crystalline polymer, i.e., the polylactic acid. Broadband dielectric spectroscopy measurements show that ultrafine nanoconfinement leads to a large elevation in glass transition temperature and a strong increment in polymer fragility index. Moreover, new relaxation time profile analyses demonstrate a spatial gradient that can be well described by either a single-exponential decay or a double-exponential decay functional form near the middle of the film with a collective interface effect. However, the dynamics at the 1-2 nanometers vicinity of the interface exhibit a power-law decay different from the single-exponential decay or double-exponential decay functional forms as predicted by theories. These results thus call for further investigations of the interface effect on polymer dynamics, especially for interfaces with perturbed chain packing.

1

^{*} Corresponding Author. Email: chengsh9@msu.edu

1. Introduction

Polymers near the interface or under nanoconfinement exhibit strong perturbations to their equilibrium dynamics and properties, including many orders of magnitude changes in structural relaxation time, shear viscosity, elastic modulus, and tens of degrees shifts in their glass transition. $^{1-19}$ Such large changes in properties have been observed in semi-crystalline polymers, 20 . 21 block copolymers, $^{22-24}$ polymer nanocomposites, $^{25-30}$ and many other nanostructured polymeric materials 31 . 32 with various engineering applications. Experiments, 2 , 5 , 13 , 14 , 17 , 29 , $^{33-41}$ computer simulations, 3 . $^{42-50}$ and theories $^{51-57}$ over the past three decades all point to a large spatial gradient of the near-interface dynamics at nanoscale vicinity of interfaces restore the bulk properties at distances of $\sim 3-5$ nm away from the interface. The large spatial gradient remains a hallmark of the interface effect, and imposes significant experimental difficulties to characterize and theoretical challenges to resolve. Similar challenges have also been confronted in the dynamics of molecular liquids and colloids near surfaces and interfaces.

Despite the wide acknowledgment of a gradient in the structural relaxation of polymers at the interface, the details of the near-interface spatial gradient in dynamics remain a topic of active discussion. For instance, the Random first-order transition (RFOT) theory⁵¹ and other entropy theories⁵⁷ predict a single exponential functional form of the spatial gradient near the interface. An interfacial layer thickness is predicted that increases with cooling and is in alignment with the increment in the sizes of the cooperatively rearranging region (CRR). The RFOT predicts a deep connection between the interface thickness, dynamics, and the bulk glass transition. On the other hand, computer simulations^{49, 58} and recent theoretical development of the Elastically Collective

Nonlinear Langevin Equation (ECNLE) theory^{55, 59, 60} showed a double exponential functional form of the spatial gradient of the interface dynamics. A characteristic interfacial layer thickness can also be identified, which is insensitive to temperature and signifies a characteristic length of the energy barrier for structural relaxation. The ECNLE theory acknowledges the spatial gradient in interfacial dynamics provides signatures of the nature of bulk glass transition. Furthermore, the computer simulations and ECNLE calculations suggest intriguing collective interface effects in the ultrathin film limit of $\sim 10 \, nm$ or below, 45 which has not yet been experimentally verified. Therefore, it is crucial to resolve the spatial gradient of the interface dynamics for the potential interface collective effect and their connecting with the bulk glassy transition.

Broadband dielectric spectroscopy (BDS) has been widely used to characterize polymer dynamics at the interface or under nanoconfinement due to its high sensitivity, wide dynamics ranges, and easy operation. $^{5,25-27,31,61-66}$ Sensing the dipolar reorientation of molecules or polymer segments, BDS measurements reflect the interface effect through an interface-induced slowing down or speeding up in structural relaxation. By assuming a phenomenological interfacial layer model (ILM), the dielectric spectroscopy measurements show interfacial layer thickness $L_{int} \sim 3-5 \ nm$ with average dynamics, $\tau_{int} \sim 10$ -100 times different from the bulk. 29,35,36 These analyses assume a step-function of the dynamics of the interface polymer that is distinct from the bulk, omitting the details of the dynamics gradient. Although the current BDS analyses support the connection between the interface dynamics and the bulk glass transition, it has a limited capacity to

differentiate the different theoretical approaches, as pointed out by a recent study.³⁴ From this perspective, new analyses enabling characterizations of the spatial gradient of the polymer dynamics at the interface are desired.

This article aims to reveal experimentally the near-interface polymer dynamics under ultrafine nanoconfinement of $\sim 10 \, nm$. Different from previous dielectric measurements of thin films,63 we focus on bulk measurements of a semi-crystalline polylactic acid with controlled distributions of amorphous phases and crystalline phases. 67-69 The new sample preparation enables a bulk sample composed of alternating stacking layers of amorphous phases of ~10 nm and crystalline lamellae phases ~7 nm in thicknesses. The unique microstructure allows new quantification of polymer dynamics under nanoconfinement from macroscopic measurements. At high temperatures, the shapes of the dielectric function change little with temperature, and the relaxation time of the amorphous phase is comparable with that of the neat polymer, suggesting a weak interface effect. Upon cooling down, strong asymmetric broadening has been observed at the low-frequency side of the dielectric spectra along with a dramatic slowing down in structural relaxation, pointing to a large interface effect and a collective interface effect. Through a new development of relaxation time distribution analyses, we can deconvolute the spectra for spatial gradients of near-interface polymer dynamics and compare them with the predictions of RFOT or ECNLE. Reasonable agreement between experiments and both theories has been observed at high temperatures, while obvious deviations has been found at 1-2 nm vicinity of the amorphous/crystalline interfaces. These results call for further investigations of the spatial gradient of the near-interface polymer dynamics, especially for polymer interfaces with perturbed chain packaging at the interface.

2. Materials and Methods

2.1 Materials.

Two types of Polylactic acid (PLA) were included in this study. The first one is an amorphous PLA (aPLA) from NatureWorks (Ingeo 4060D), and the second one is a semi-crystalline poly(L-lactic acid) (sPLA, LX530 from Total Energies Corbion). The molecular weight of aPLA and sPLA were obtained at ambient conditions through size exclusion chromatography (SEC) in tetrahydrofuran (THF) that was calibrated using polystyrene standards. For aPLA, the weight average molecular weight is 173 kg/mol with a polydispersity index of 1.68. For sPLA, the weight average molecular weight is 98 kg/mol with a polydispersity index of 1.7.

2.2 Preparation of asPLA with controlled distributions of crystalline phases and amorphous phases.

Uniaxial extension at temperatures close to the glass transition temperature, T_g , of sPLA followed by thermal annealing for crystallization were employed to control the spatial distributions of the crystalline and the amorphous phases, following recently published protocols. Specifically, aPLA and sPLA thin films of $50.8 \, mm \times 25.4 \, mm \times 0.3 \, mm$ (length × width × thickness) were pressed molded at temperatures at $T=473 \, K$ and quenched down to $T=293 \, K$ by a direct contacting the hot films with a large cold aluminum plate. The whole cooling process finishes in about $30 \, s$ that corresponds to a cooling rate of $\sim 6 \, K/s$. The amorphous sPLA films were subjected to uniaxial extension at $T=343 \, K$ in an Instron floor model 5982 equipped with an environmental chamber.

The temperature accuracy of the oven is $\pm 0.1 \, K$. A constant crosshead speed of 5 mm/min was applied and an elongation ratio $\lambda = 4$ was achieved, which corresponds to an effective Hencky deformation rate of $0.0033 \, s^{-1}$ at the beginning of the deformation and $0.0008 \, s^{-1}$ at the end of deformation. The effective terminal relaxation time of sPLA is $\tau_d \approx 1,600 \, s$ at $T = 343 \, K$ (see Supplementary Materials (SM) for the estimation and the linear viscoelastic spectra of sPLA of Figure S1). Thus, the applied constant crosshead speed of 5 mm/min at T=343~K gives a Weissenberg number $Wi_d=\dot{\varepsilon}\tau_d>$ 1 at the end of deformation that ensures effective chain deformation during the predeformation step.68 The stretched films were then annealed at 373 K for 60 minutes and 403 K for another 60 minutes to ensure sufficient time for crystallization of the uniaxially oriented sPLA. We chose these two temperatures for thermal annealing because the fastest rate of cold recrystallization of this sPLA takes place at T = 373 K (see Figure **S2** of SM) and our measurements goes to as high as $T = 403 \, K$. Thus, annealing at $T = 403 \, K$. 373 K promotes the re-crystallization and annealing at 403 K avoids any further microstructures changes during the heating and cooling of dynamics measurements. We note that the annealing step converts the sPLA film from an amorphous state to semicrystalline, which is named asPLA in the following context. In particular, the crystallization during annealing preserves the deformation of chain network of sPLA, which introduces the unique morphology of alternating packing layers. Note that the same protocol does not work for aPLA due to the active stress relaxation of deformed amorphous polymer upon annealing at high temperatures. 70 Figure 1 provides a sketch of the sample preparation of asPLA.

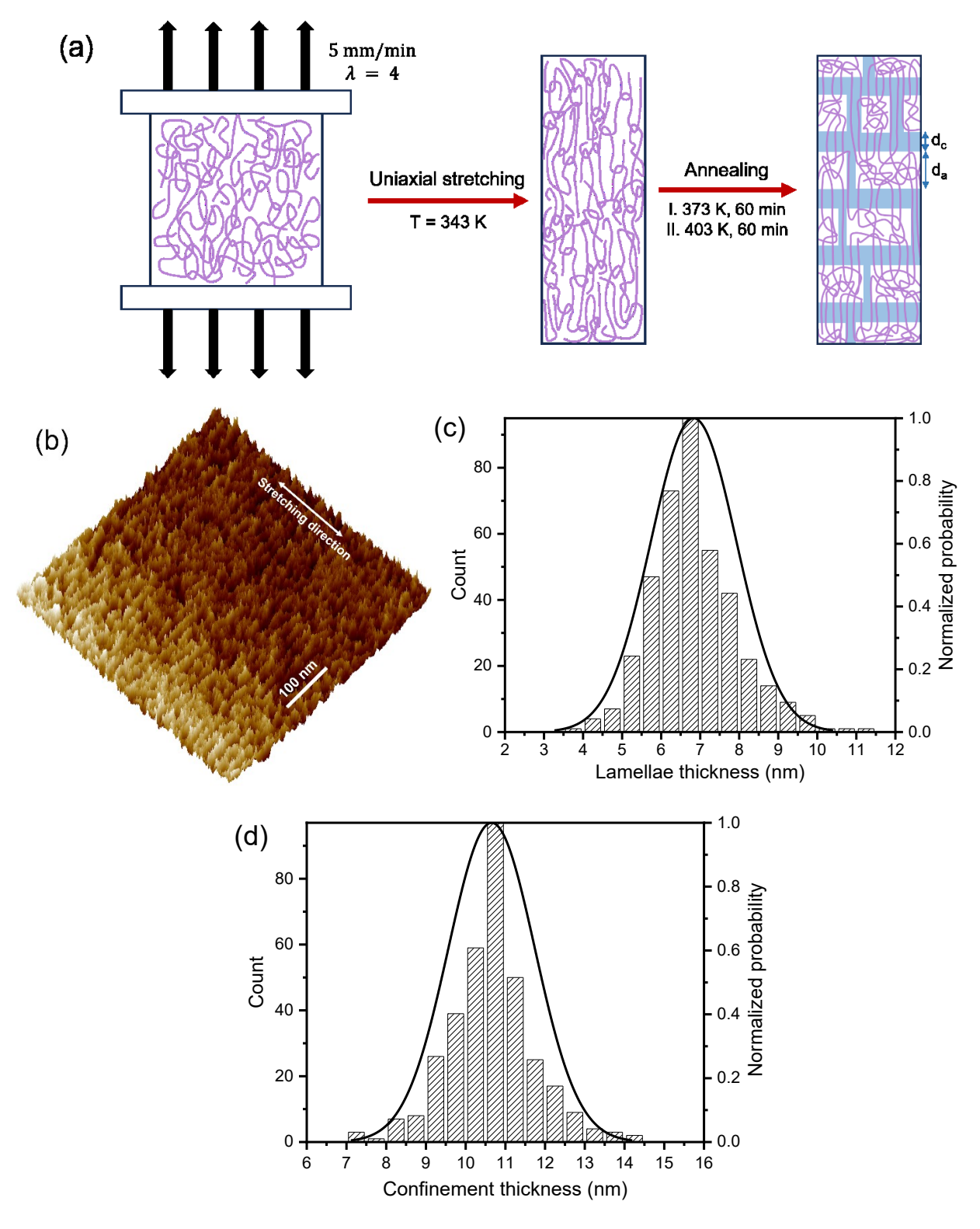


Figure 1. (a) A sketch of the sample preparation that involves pre-deformation close to the glass temperature of the sPLA followed by a thermal annealing to control the spatial distribution of the amorphous phases and the crystalline phases of semicrystalline polylactic acid (sPLA). The pink lines are representative polymer chains, the light blue stacks are the crystalline phases. d_c is the lamellae thickness and d_a the thickness of the amorphous phases. The crystalline phases and

the amorphous phases are stacked in an alternating way parallel to the stretching direction. (b) Atomic force microscopy (AFM) measurements of the adhesion map that shows the surface morphology (3D visualization) of the asPLA. The ridges are the crystalline phases and the darker valley between the ridges are the amorphous phases. The AFM measurements thus suggest an crystalline/amorphous alternating microstructure. (c) A historgram analysis of the distribution of lamellae thickness from the AFM measurements. The solid line is a fit to normal distribution that gives a mean $\mu=6.8~nm$ and a standard deviation $\sigma=1.1~nm$. The polydispersity index (PDI) is 1.03. (d) A historgram analysis of the distribution of the sizes of the amorphous domain, i.e. the nanoconfinement, from the AFM measurements. The solid line represents a fit of the historgrams to a normal distribution with a mean $\mu=10.6~nm$ and a standard deviation $\sigma=1.1$. The polydispersity index (PDI) is 1.01. The details of the calculation of the polydispersity index is given in Supplementary Materials.

2.3 X-ray scattering.

Small-angle x-ray scattering (SAXS) and wide-angle x-ray diffraction (WAXD) of asPLA was performed at the Soft Matter Interfaces (12-ID) beamline at the Brookhaven National Laboratory. A strip sample with a thickness of ~ 0.15 mm was loaded onto a sample holder with a length in the vertical direction that is parallel to the deformation direction. We perform SAXS and WAXD measurements at six different locations of the same film to ensure the consistency of the acquired two-dimensional (2D) scattering patterns. The distance between the sample and the detector was set to be 8.3 meters, and the radiation wavelength used was $\lambda = 0.77$ Å. The scattered X-rays were captured using an in-vacuum Pilatus 1M detector, which consists of an array of 0.172 mm square pixels in a 941×1043 configuration. The raw 2D-SAXS and 2D-WAXD images were converted into Q-space (the wavevector space), visualized in Xi-CAM software, and then radially integrated using a customized Python code.

2.4 Differential scanning calorimetry (DSC).

The melting temperature, T_m , and the crystallinity of the asPLA was characterized with differential scanning calorimetry (DSC, TA instrument Discovery Q50) at a heating

and cooling rate of 2 K/min from 293 K to 473 K and from 473 K to 293 K. The first circle is recorded to determine the effect of pre-deformation of the asPLA. The second heating helps determine the temperatures for cold recrystallization of sPLA (**Figure S2**). A thin film of asPLA was loaded onto an aluminum pan with close contact with the flat bottom of the pan before a pan lid was placed. The T_m was determined through the peak temperature of the melting process in the specific heat capacity, C_p , curve.

2.5 Broadband dielectric spectroscopy (BDS).

Broadband dielectric spectroscopy (BDS) measurements were performed to characterize the glassy dynamics of asPLA on a Novocontrol Concept-40 system with an Alpha-A impedance analyzer and a Quatro Cryosystem temperature control system. The temperature accuracy is $\pm 0.1\,K$. The applied amplitude of the voltage is $1\,V$ and the frequency is 10^7 – $10^{-2}\,Hz$. An asPLA film of a thickness of 0.15 mm was sandwiched by two gold electrodes of a diameter of 20 mm. No spacer was needed in the measurements. The temperature range was set from 293 K to 403 K and the BDS measurements were performed upon cooling from 403 K to 293 K at an interval of 5 K and upon heating from 293 K to 403 K at an interval of 10 K. Little changes to the dielectric spectra were observed during the heating or cooling of the measurements at the same temperature (see **Figure S3** of the SM), confirming the absence of further crystallization of asPLA during the dynamics measurements.

2.6 Atomic force microscope (AFM).

The AFM measurements were conducted to characterize the surface morphology using a Dimension FastScan atomic force microscope system with ScanAsyst (BRUKER) at room temperature. ScanAsyst_air cantilever (BRUKER) with spring constant of 0.4 N/m and silicon tip on nitride lever with a radius of 2 nm were used. The scan rate is 0.994 Hz and the image data is collected as adhesion force (**Figure 1b**).

3. Results and Discussions.

3.1 The structure of the asPLA.

Figure 2a presents the specific heat capacity, C_p , of the asPLA with a sharp melting peak at T = 436 K along with a shoulder peak at a few degrees lower. The appearance of a shoulder peak of asPLA could be due to various crystalline forms or due to different lamellae thickness. Since the WAXD measurements (Figure S4) of asPLA show the dominating α form of PLA⁷¹ and little signs of other crystalline forms, we attribute the shoulder peak to the slightly different lamellae thicknesses. The enthalpy upon melting, $\Delta H \approx 42.3 \, J/g$, which corresponds to a crystallinity of $\frac{\Delta H}{\Delta H^{\infty}} \approx 45\%$ for asPLA where $\Delta H^{\infty} = 93 \, J/g$ is the equilibrium enthalpy of melting. This high crystallinity also explains the weak signature of a glass transition in the DSC measurement. In addition, the DSC measurement at the slow heating rate (2 K/min) can also help estimate the lamellae thicknesses, d_c , through Gibbs-Thomson relation: $T_m = T_m^{\infty} \left(1 - \frac{2\sigma_e}{\rho \Delta H_f^0 d_c}\right)$, where $T_m pprox 436\,\mathrm{K}$ is the peak melting temperature of asPLA, T_m^∞ is the equilibrium melting temperature, σ_e is the surface energy of the basal plane of the lamellae, and ρ is the mass density of the crystalline phase. For asPLA, $T_m^{\infty}=480~K,~\sigma_e=3.6~\times 10^{-20}~J/nm^2,~{\rm and}$ $ho = 1.24 \ g/cm^3.^{72, 73}$ This gives a rough estimate of the average lamellae thickness,

 $d_{c,DSC} \approx 6.9 \, nm$ that is very close to the lamellae thickness of $d_{c,AFM} \approx 6.83 \, nm$ (Figure 1c) from the AFM measurements. Given the one-on-one correspondence of the melting temperature and the lameallae thickness, the sharp melting peak suggests a narrow distribution of the lamellae thickness (also see Figure S5 and SM for more discussions about the estimate of the distribution of lamellae thickness from DSC measurements).

To further characterize the lamellae thickness and the microstructure of the asPLA, we turned to small angle x-ray scattering (SAXS) that provide direct characterizations of the lamellae thicknesses. The Inset of **Figure 2b** shows the two-dimensional (2D) SAXS spectra of the asPLA. A sharp scattering peak appears at the azimuth direction with little scattering in the equator of the 2D-SAXS spectra, supporting a strong stacking of the lamellae along the stretching direction (see the sketch of **Figure 1a** and the AFM images of **Figure 1b**). **Figure 2b** presents the $I(Q)Q^2$ vs Q, where I(Q) is the scattering intensity along the stretching direction. It has a sharp scattering peak around scattering wavevector $Q^* \approx 0.036 \, \text{Å}^{-1}$ signifying a strong correlation among neighboring lamellae.

One can further compute the one-dimensional correlation function, K(d), with d a length scale:⁷⁴

$$K(d) = \int_0^\infty Q^2 I(Q) \cos(Qd) dQ / \int_0^\infty Q^2 I(Q) dQ$$

which provides quantification of the lamellae thickness, $d_{c,SAXS}$, the long period, L, and the thickness of the amorphous phase between two neighboring lamellae, $d_a = L - d_{c,SAXS}$. **Figure 2c** gives the K(d) of the asPLA, from which one can identify $d_{c,SAXS} = 6.7 \, nm$ that is very close to $d_{c,DSC} \approx 6.9 \, nm$ and AFM measurements. Note that even perfect step-function-type density profiles do not give a step function in the correlation function, K(d).⁷⁵ Thus, one should not read the polydispersity of the lamellae thickness

directly from the broaden of the correlation peaks of the K(d). In addition, the SAXS gives $L=17.3\ nm$ for asPLA, which leads to $d_a=10.6\ nm$ that is in excellent agreement with the sizes of the amorphous domains from the AFM measurements (Figure 1d). The lamellae thickness and the long-period of asPLA agree well with previous SAXS studies of semi-crystalline PLLA under similar sample preparation conditions.⁶⁸ The SAXS measurements thus point to an alternating stacking layered structures of the crystalline and amorphous phases of asPLA, in consistent with the AFM measurement. We would like to emphasize that although large sections of layering structures of crystalline phase/amorphous phases has been observed, there are small amounts of defects in the layered structures of asPLA. However, we do not believe these defects could have a major influence on the interpretation of the dynamics measurements. The amorphous polymer is thus under planar nanoconfinement. Since the amorphous phase of asPLA is composed primarily of tie chains or tie-entanglements with potential influence from the chain orientation during the pre-deformation step, the chain packing at the interface resembles a high-density surface grafting rather than that of physical sorption as in conventional capped thin films. The obtained crystalline/amorphous alternating phases of asPLA provide nanoconfinements are thus different from conventional capped thin films, which might have profound influences to polymer dynamics. Importantly, the thickness of the amorphous phase is $\sim 10.6 \, nm$, falling into an ultrafine nanoconfinement region that has not been well-characterized. Thus, the new sample preparation enables preparations of polymers under ultrafine nanoconfinement with narrow distribution of the degree of nanoconfinement.

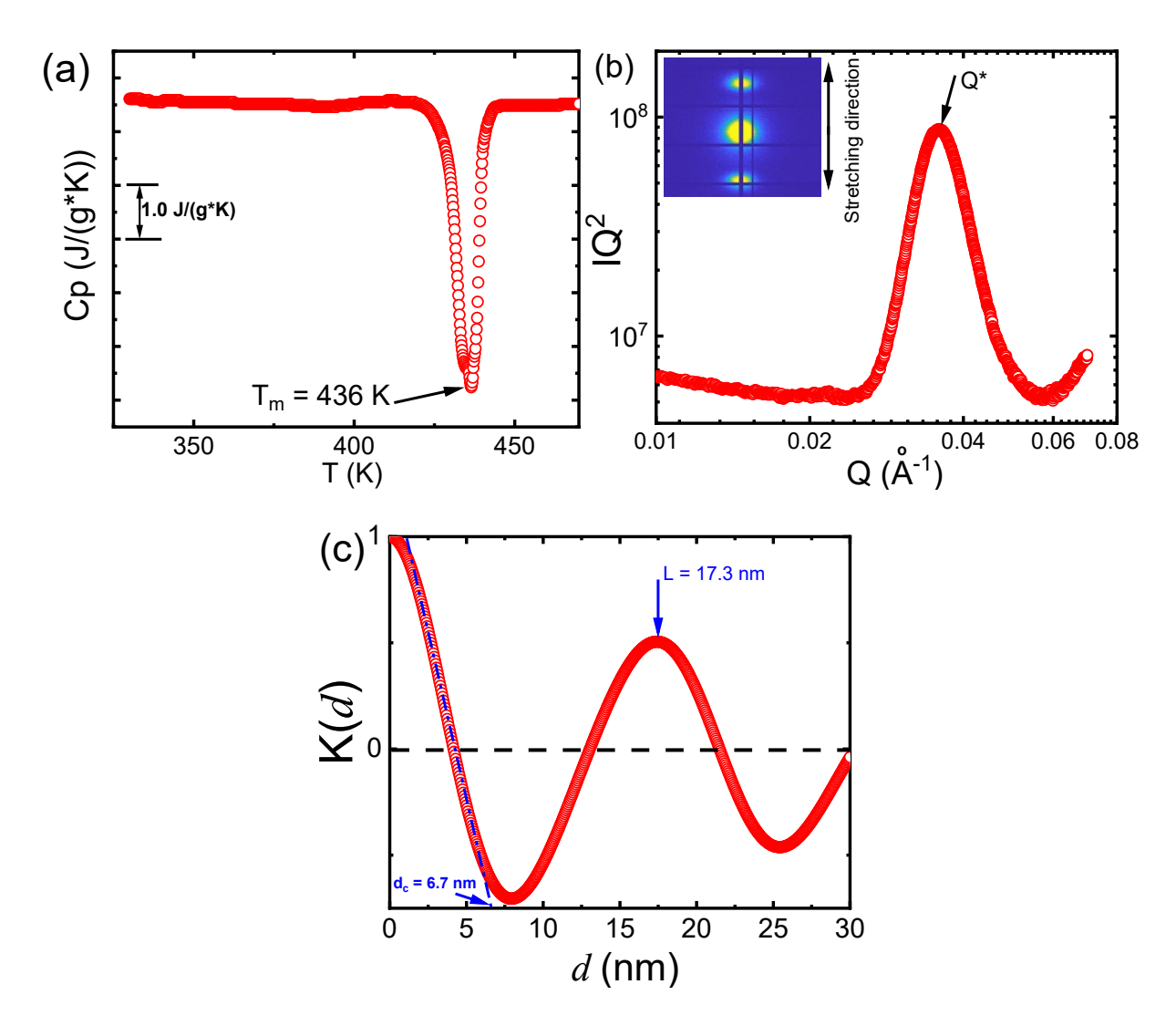


Figure 2 (a). The specific heat capacity, C_p , of asPLA from differential scanning calorimetry (DSC) measurements. The data is from the first heating circle. (b). IQ^2 vs Q of asPLA, where I is the scattering intensity along the azimuth direction of the 2D scattering pattern (the inset image) of the small angle x-ray scattering (SAXS). (c) 1-D correlation function from the SAXS spectra, where d_c is the lamellae thickness, L is the long-period.

3.2 The dynamics of the asPLA.

Figure 3 presents the dielectric spectra of the asPLA (**Figure 3a**), and the aPLA (**Figure 3b**) at different temperatures. The insets of **Figure 3a** and **Figure 3b** provide their normalized spectra to capture the spectra shapes. Several features are worth noting: (i) The segmental peak of asPLA broadens significantly upon cooling from 383 K to 343 K. More importantly, the dielectric broadening of asPLA upon cooling seems to take

place primarily at the low-frequency side (Figure 3a). The strong asymmetric dielectric broadening over a small temperature changes of 40 K is remarkable. Importantly, the density changes of the amorphous phases in asPLA upon temperature changes should be comparable to that of the aPLA, which does not exhibit any changes in the shape parameters of their dielectric functions upon cooling. On the other hand, the volumetric expansion coefficient of amorphous PLA is ${\sim}8\times10^{-4}~K^{-1}$, one should anticipate ${\sim}3\%$ volume changes from 383 K to 343 K. Such volume changes should not change the shape parameters of dielectric functions according to the dielectric measurements of polymers at different temperatures or at high pressures. Furthermore, the thermal shrinkage of amorphous phases from 383 K to 343 K should speed up their characteristic relaxation time (due to more free-volume), which has not been observed. Thus, the thermal shrinkage induced volume changes should not play a major role in the observed asymmetric dielectric broadening. The observed strong asymmetric broadening upon cooling should be due to an interface effect. 36, 38, 39 On the other hand, the shapes associated with the segmental relaxation peaks of aPLA do not change with temperature, and a master curve can be constructed (the solid black line in the inset of Figure 3b). (ii) An envelope can be identified for dielectric spectra of asPLA at high temperatures (the black line in the inset of Figure 3a), indicating a weak influence of the amorphous/crystalline interface to dynamics at these high temperatures. (iii) The envelope spectra of asPLA (the solid black line) at high temperatures are much broader than the neat aPLA (the dashed grey line) as shown in the inset of Figure 3a, highlighting a more heterogeneous dynamics of the asPLA. At this moment, we are not sure about the origin of the broader dielectric spectra of asPLA than aPLA at high temperatures. One

possibility is that the pre-deformation and following-up thermal annealing leads to slightly different chain packing of asPLA from aPLA. (iv) The characteristic segmental relaxation times of the amorphous phase of asPLA, τ_{α}^{asPLA} , identified from the peak positions are substantially slower than that of the aPLA, τ_{α}^{asPLA} , especially at low temperatures (Figure 4). Note that we identify τ_{α}^{asPLA} from the fastest segmental modes of the amorphous phase since dielectric broadening occurs only at low frequencies. τ_{α}^{asPLA} is comparable with τ_{α}^{aPLA} at high temperatures of $\sim 383~K$, supporting a negligible interface effect in the high-temperature spectra of asPLA. Interestingly, τ_{α}^{asPLA} becomes significantly larger than τ_{α}^{aPLA} with cooling, highlighting the influence of amorphous/crystalline interface to the fastest modes, i.e. the amorphous polymers at the middle plane (Figure 5). This suggests the emergence of a collective interface effect upon cooling. The collective interface effect has been observed in computer simulations and been predicted by theory 45, while experimentally verification of the collective interface effect falls behind.

To be more quantitative, we fit the temperature dependence of τ_{α}^{asPLA} and τ_{α}^{aPLA} to the Vogel-Fulcher-Tammann (VFT) relation: $\tau_{\alpha}(T) = \tau_0 \exp(\frac{B}{T-T_0})$ with τ_0 , B, and T_0 being the fit constants. One can obtain the glass transition temperature T_g , fragility index $m = \frac{\partial log \tau_{\alpha}}{\partial (\frac{T}{T})}|_{T=T_g}$ and the Vogel temperature T_0 . The fit parameters are presented in **Table 1**, where the T_g of asPLA is $\sim 10~K$ higher than that of the aPLA. This is consistent with the general observation that the interface effect could lead to a higher T_g . Interestingly, the observed $\sim 10~K$ shift in T_g in asPLA is much larger than the $\sim 3-5~K$ shift in T_g of polymer nanocomposites with comparable particle size of diameter around 20 nm. $^{28, 79}$ In addition, the fragility index of asPLA is around 194 from the BDS measurement which is

much larger than that of 155 of aPLA. Moreover, the pre-deformation and the subsequent annealing change the Vogel temperature from 294 K of aPLA to 312 K of asPLA. All these are large changes in dynamics properties of the asPLA compared with the aPLA and they are signatures of a strong collective interface effect in the ultrafine nanoconfined system. In the discussions, the collective interface effect is referred as the synergistic effect of neighboring amorphous/crystalline interfaces on the confined amorphous polymer.

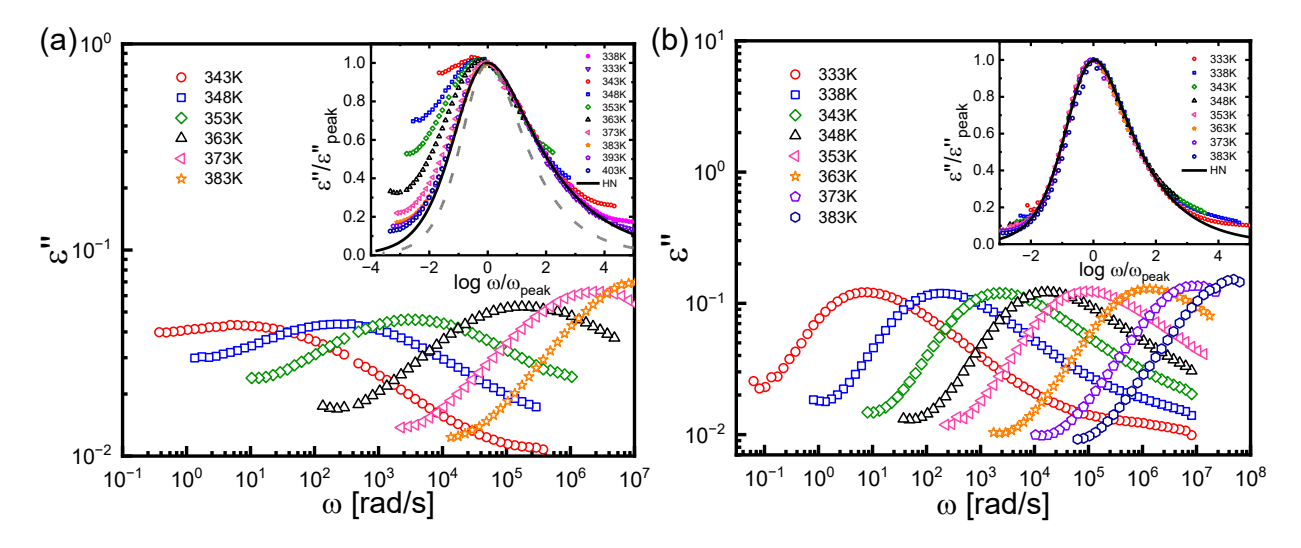


Figure 3. Dielectric loss permittivity, ε'' , of (a) asPLA and (b) aPLA at different temperatures. The inset of (a) and (b) provides the normalized spectra of $\varepsilon''/\varepsilon''_{peak}$ vs ω/ω_{peak} where ω_{peak} is the angular frequency associated with ε''_{peak} , the peak amplitude of the loss permittivity The solid lines in (a) and (b) represent the Havriliak-Negami (HN) functions that fit to the envelope of the corresponding normalized spectra. The grey dashed line is the normalized spectra of the aPLA.

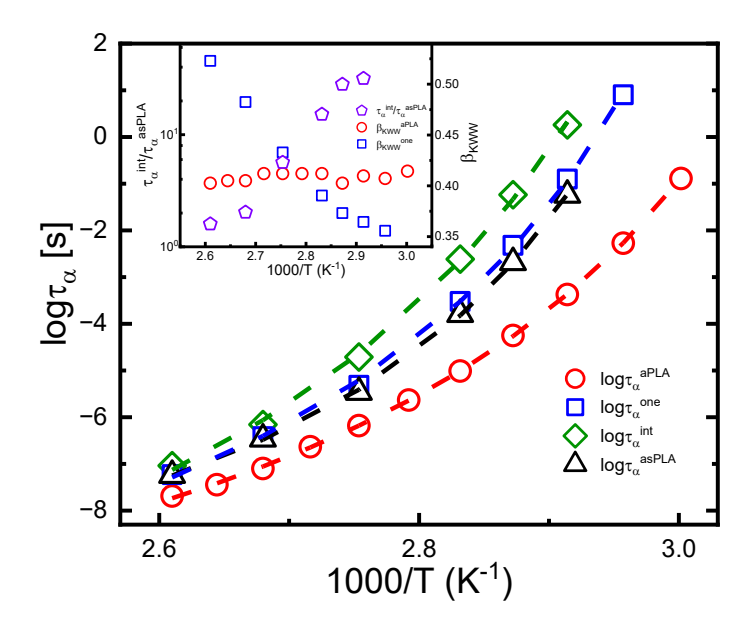


Figure 4. The Vogel-Fulcher-Tammann plot of the characteristic relaxation times of the dielectric analyses. τ_{α}^{aPLA} : the segmental relaxation time of the aPLA. τ_{α}^{asPLA} : the segmental relaxation time of the non-interface polymer. τ_{α}^{int} : the segmental relaxation time of the interface polymer in the interfacial layer model analysis (see section 3.3). τ_{α}^{one} : the characteristic relaxation time of the asPLA in the one-HN function analysis (see section 3.3). The inset shows the ratio of $\tau_{\alpha}^{int}/\tau_{\alpha}^{asPLA}$ and the Kohrauch-Williams-Watts (KWW) stretching parameter, β_{KWW} , of asPLA and the aPLA.

Table 1. A summary of the fit parameters of the fit of relaxation times to VFT relation

τ (s)	$log au_0$	B (K)	$T_0(K)$	$T_g(K)$	m
$ au_{lpha}^{aPLA}$	-13.1	1108	294	326	155
$ au_{lpha}^{one}$	-13.3	1077	305	336	168
$ au_{lpha}^{int}$	-14.6	1373	303	339	156
$ au_{lpha}^{aspla}$	-12.0	779	312	336	194

3.3 The interface effect.

To better quantify the interface effect, we first utilize an interfacial layer model (ILM) (**Figure 5a** and Section 3.3.1) that treats the interface a separate capacitor in parallel connecting with the amorphous phases away from the interface. This method provides the average interfacial dynamics and characteristic interfacial layer thicknesses. In Section 3.3.2, we developed a new analysis that takes into account the elementary relaxation mode of PLA, and enables fine deconvolution of the dielectric spectra for a

detailed spatial gradient at the interface (**Figure 5b**). In both analyses, we assume monodispersity of the amorphous region of $d_a=10.6\,nm$. Experimentally, d_a has a polydispersity index of ~ 1.01 according to the AFM measurements. Therefore, we do not anticipated a major influence of the polydispersity of the nanoconfinement to our discussions about the interfacial dynamics in the following sections.

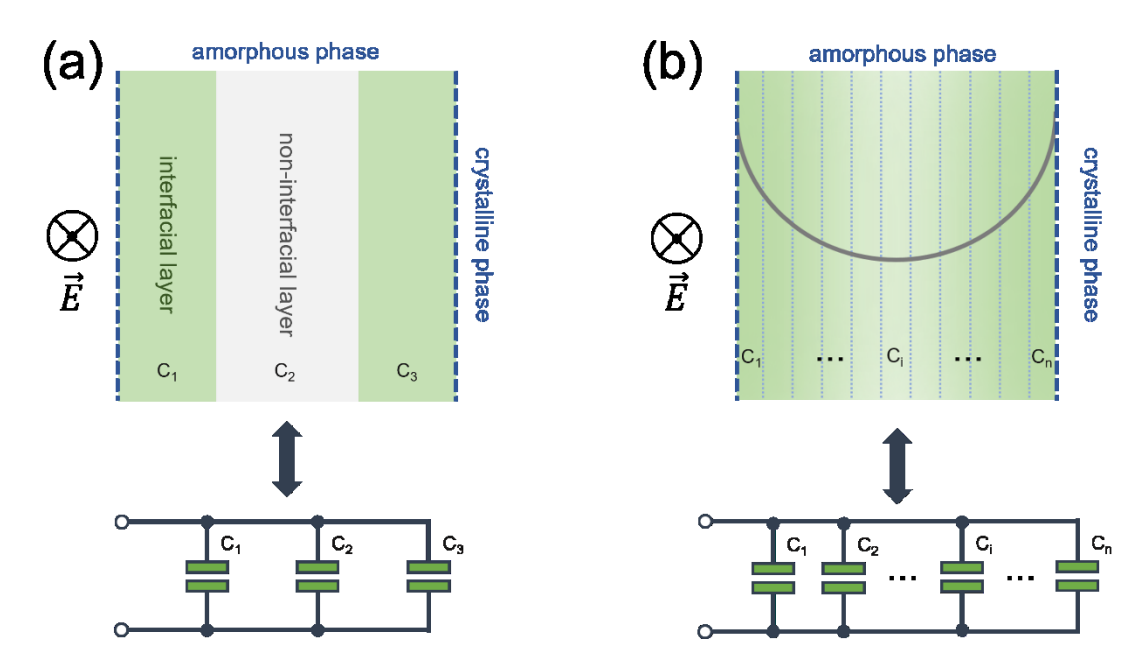


Figure 5. The illustrations of (a) an interfacial layer model (ILM) model and (b) a spatial gradient fingerprinting analysis. In the ILM, the dielectric response is ascribed as the interfacial layer and non-interfacial layer, which are treated as separate capacitors C_1 , C_2 , and C_3 connecting in parallel, where $C_1 = C_3$ due to symmetry. In the spatial gradient fingerprinting analysis, the dielectric spectrum is modeled as the sum of many capacitors, C_i with i=1 to n, connecting in parallel and $C_i = C_{n+1-i}$ due to symmetry. The color gradients and the solid line in **Figure 5b** represent the dynamics gradient, where a darker green refers to a slower dynamics layer. In the dielectric measurements, the applied electric field, \vec{E} , is perpendicular to the sample plane.

3.3.1 The interfacial layer model (ILM) analysis

The unique crystalline/amorphous alternating layering structure of the asPLA offers an opportunity to quantify the interface effect. The Kuhn length of the PLA is $l_k \approx 1.28~nm$ is much smaller than the thickness of the amorphous phase, $d_a \approx 10.6~nm$. One

can model the total dielectric response of asPLA through parallel capacitors (**Figure 5a**) of the non-interface polymer, the interface polymer, and the crystalline phases:

$$\varepsilon_t^*(\omega) = \varepsilon_n^*(\omega)\varphi_n + \varepsilon_{int}^*(\omega)\varphi_{int} + \varepsilon_c^*(\omega)\varphi_c + \varepsilon_\infty + \frac{\sigma_{dc}}{i\varepsilon_0\omega}$$
 (1)

where $\varepsilon_t^*(\omega)$, $\varepsilon_n^*(\omega)$, $\varepsilon_{int}^*(\omega)$, and $\varepsilon_c^*(\omega)$ are the complex dielectric permittivity of the asPLA, the non-interface part of the asPLA, the interface layer of the asPLA, and the crystalline phase of asPLA, φ_n , φ_{int} , and $\varphi_c=0.45$ are the volume fractions of the non-interface part, the interface layer, and the crystalline phase of the asPLA, and ω is the angular frequency. σ_{dc} is the dc-conductivity, ε_0 is the vacuum permittivity, and ε_∞ is the dielectric permittivity at infinite frequencies. Similar analyses have been proposed recently for polymers under nanopore confinement. Since there is negligible dielectric loss of the crystalline phase of the asPLA in the temperature and frequency range of the measurements, we group $\varepsilon_c^*(\omega)\varphi_c + \varepsilon_\infty$ as one contribution to the real part of the complex permittivity in the analyses. Experimentally, the total dielectric amplitude of the asPLA, $\Delta\varepsilon_{asPLA}\approx 0.33$ holds at the testing temperatures that is very close to the $\Delta\varepsilon\approx 0.30$ accounting for 55% of that of the aPLA, $\Delta\varepsilon_{aPLA}\approx 0.54$ at the same temperatures (**Figure S6**). Thus, the dielectric measurements give crystallinity of asPLA very close to $\varphi_c=45\%$ from DSC measurements.

Figures 6a and 6b present the loss permittivity spectra, $\varepsilon''(\omega)$, and the derivative of the storage permittivity, $\varepsilon'_{der}(\omega) = -\frac{\pi}{2} \frac{\partial \varepsilon'(\omega)}{\partial ln\omega}$, of the asPLA at T=363~K. The dashed pink lines, the dash-dotted blue lines, and the dotted orange lines in the main frame represent $\varepsilon^*_n(\omega)$, $\varepsilon^*_{int}(\omega)$, and the Maxwell-Wagner-Sillars (MWS) polarization process, respectively. We model them with Havriliak-Negami (HN) functions: $\varepsilon^*(\omega) = \frac{\Delta \varepsilon}{(1+(i\omega\tau_{HN})^\beta)^\gamma}$.

with $\Delta\varepsilon$ being the dielectric amplitude, τ_{HN} the HN time, and β and γ the shape parameters. Specifically, we take $\varepsilon_n^*(\omega)$ with the same shape parameters as the envelope spectra in the inset of **Figure 3a**. Note that the MWS polarization process (the dotted orange lines) has little influence on the discussions of molecular dynamics due to the large separation between MWS and $\varepsilon_{int}^*(\omega)$. The solid black lines are a sum of all three processes. In addition, the insets of **Figures 6a** and **6b** show the one-HN function analysis (the dashed green lines) plus an MWS process (the dotted orange lines) that can also describe the spectra reasonably well. The characteristic relaxation times from the one-HN analysis are τ_α^{one} .

The temperature dependences of τ_{α}^{int} (the olive diamonds) and τ_{α}^{one} (the blue squares) are also provided in **Figure 4** for a direct comparison with τ_{α}^{asPLA} and τ_{α}^{aPLA} . Interestingly, τ_{α}^{one} follow similar temperature dependence as τ_{α}^{asPLA} . On the other hand, τ_{α}^{int} shows much stronger temperature dependence than τ_{α}^{asPLA} . The stronger temperature dependence of τ_{α}^{int} than τ_{α}^{asPLA} can also be reflected by the high ratio of $\tau_{\alpha}^{int}/\tau_{\alpha}^{asPLA}$ upon cooling (the inset of **Figure 4**). The HN function shape parameters connect with the Kohlrausch-Williams-Watts (KWW) parameter: $\beta_{KWW} = (\beta\gamma)^{1/1.23}$. As shown in the bottom inset of the **Figure 4**, β_{KWW} of asPLA (blue squares) drops significantly from ~0.48 at T = 373 K to ~0.35 at 333 K, while little changes of β_{KWW} are observed for aPLA (red circles). All these analyses are characteristics of the collective interface effect on polymer dynamics.

The above analysis can also provide insights into the characteristic thicknesses of the interfacial layer through $L_{int}(T) = \frac{1}{2}L * \varphi_{int}(T)$ (**Figure 6c**). The $\varphi_{int}(T)$ and $\varphi_n(T)$ are presented in the inset of **Figure 6c**. This leads to an estimate of $L_{int}(T)$ that changes

from $L_{int} \sim 1.5~nm$ at T=383~K (1.14 T_g) to $L_{int} \sim 3.0~nm$ at T=343~K that is around 10~K above T_g . The $L_{int} \sim 1.5~nm$ of PLA with characteristic ratio, $C_{\infty}=6.9$, at $T=1.14~T_g$ agrees with previous results of PNCs, where polymer matrices with $C_{\infty}=6-7$ has $L_{int} \sim 1.6 \pm 0.5~nm$ when forming nanocomposites.³⁵

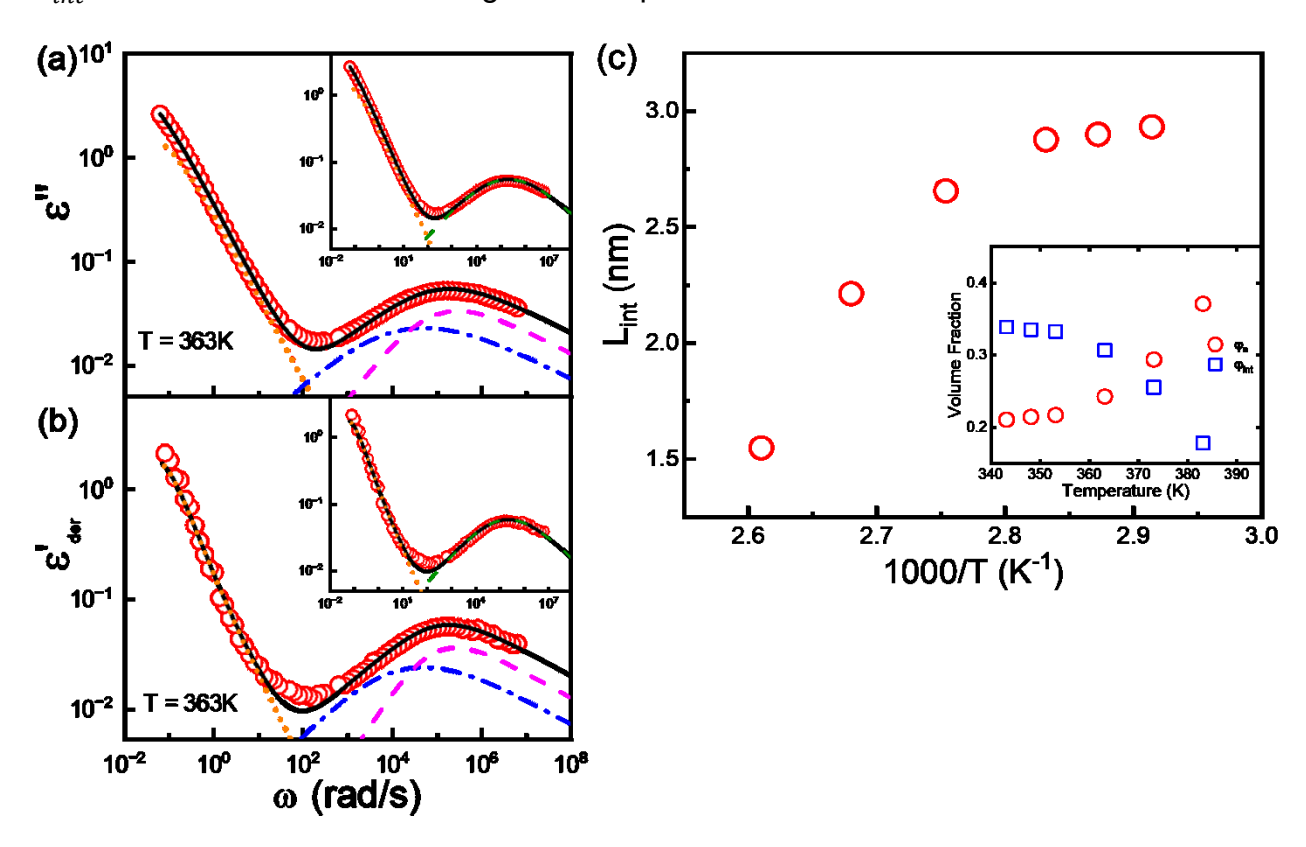


Figure 6. The interfacial layer model analysis to the dielectric spectra of the asPLA. (a) The dielectric loss permittivity, $\varepsilon''(\omega)$. (b) The derivative spectra of the dielectric storage permittivity, $\varepsilon'_{der}(\omega)$. The pink dashed lines, the blue dash-dotted lines, and the orange dotted lines are the corresponding dielectric functions of the non-interface polymer, $\varepsilon''_{int}(\omega)$, the interface polymer, $\varepsilon''_{int}(\omega)$, and the MWS processes in the main frame of (a) and (b). The insets of panels (a) and (b) provide the corresponding one-HN function fit (the green dashed line) to the same spectra. An MWS polarization process (the orange dotted line) is also included in the one-HN function analysis. (c) The characteristic interfacial layer thickness, L_{int} , of the ILM analysis. The inset of **Figure 6c** provides the corresponding volume fraction of the interface polymer, φ_{int} , and the non-interface polymer, φ_n .

3.3.2 Fingerprinting the spatial gradient of near-interface polymer dynamics.

The empirical ILM analysis provides average dynamics of the non-interface polymer and the interface polymer that can hardly distinguish different theoretical

approaches.³⁴ New analyses to fingerprint the spatial gradient of interfacial dynamics are required. The dielectric spectra of the asPLA can be modeled as (see **Figure 5b**):

$$\varepsilon_t^*(\omega) = \frac{1 - \varphi_c}{d_a} \int_0^{d_a} \varepsilon^*(z; \omega) dz + \varepsilon_c^*(\omega) \varphi_c + \varepsilon_\infty + \frac{\sigma_{dc}}{i\varepsilon_0 \omega}$$
 (2)

where $\varepsilon^*(z;\omega)$ is the dielectric function of asPLA at a distance z away from the amorphous/crystalline interface. The $\varepsilon^*(z;\omega)$ can be modeled through a location-specific HN function, $\varepsilon^*(z;\omega) = \frac{\Delta \varepsilon_z}{\left(1+(i\omega\tau_{HN,z})^{\beta_z}\right)^{\gamma_z}}$, with $\Delta \varepsilon_z$, β_z , and γ_z being the corresponding dielectric amplitude and shape parameters. First approximations of $\Delta \varepsilon_z$, β_z , and γ_z are the $\varepsilon^*_n(\omega)$, the basic dielectric function of asPLA in the absence of interface effect. This leaves $\tau_{HN,z}$ the only set of free parameters, which carries the spatial gradient of segmental dynamics.

Furthermore, dz/d_a represents the volume fraction of the asPLA with characteristic dynamics of τ_z of the amorphous phase. One can then rewrite dz/d_a as $dz/d_a=g(ln\tau_z)dln\tau_z$ with $g(ln\tau_z)$ the relaxation time distribution density function of τ_z . Therefore,

$$\varepsilon_t^*(\omega) = (1 - \varphi_c) \int_{-\infty}^{+\infty} \frac{\Delta \varepsilon_z * g(\ln \tau_z)}{\left(1 + \left(i\omega \tau_{HN,z}\right)^{\beta_z}\right)^{\gamma_z}} d\ln \tau_z + (\varepsilon_c^*(\omega)\varphi_c + \varepsilon_\infty) + \frac{\sigma_{dc}}{i\varepsilon_0 \omega}$$

$$\tau_{HN,z} = \tau_z \left[\tan(\frac{\pi}{2(\nu_z + 1)}) \right]^{1/\beta_z}$$
(4)

where $\int_{-\infty}^{+\infty} g(ln\tau_z)dln\tau_z = 1.0$, $\Delta\varepsilon_z = \Delta\varepsilon$ of the $\varepsilon_n^*(\omega)$, $\beta_z = \beta = 0.6$, and $\gamma_z = \gamma = 0.3$ are pre-determined from $\varepsilon_n^*(\omega)$, and $(\varepsilon_c^*(\omega)\varphi_c + \varepsilon_\infty)$ is a constant. The conductivity relaxation is far from the polymer dynamics in asPLA and thus does not influence the calculation for relaxation time distribution of the amorphous polymer phase. We employ the generalized

regularization method to compute the $g(ln\tau_z)$,⁸⁰ from which the contribution of τ_z to the the total dielectric spectra can be obtained. A fundamental difference between **Eqns. 3** and **4** and the previous relaxation time distribution analyses of polymer nanocomposites^{35, 36, 38, 39} is a preservation of the HN function form that allows a more accurate account for the elementary relaxation mode of the matrix polymer.

Figure 7a presents $\Delta\varepsilon*g(ln\tau_z)$ vs $ln\tau_z$ of asPLA at three temperatures: T=363~K, T=353~K, and T=348~K. There is an obvious broadening of the relaxation time distribution upon cooling. The peak amplitude of the relaxation time distribution function reduces upon cooling. These features are consistent with the increment in broadening in the dielectric dispersion at the frequency domain. The inset of Figure 7a gives $W(ln\tau_z) = \int_{-\infty}^{ln\tau_z} \Delta\varepsilon*g(ln\tau_z)dln\tau_z = \int_{-\infty}^{ln\tau_z} g(ln\tau_z)dln\tau_z$ that accounts for the accumulated fractions of the dielectric contribution of polymer exhibiting relaxation time shorter than τ_z . The dashed lines are the location of the relaxation time associated with τ_α^{asPLA} . In principle, the relaxation time distribution spectra should start from τ_α^{asPLA} since τ_α^{asPLA} is the fastest segmental relaxation mode. However, the high-frequency tail of the spectra may be affected by sub-segmental dynamics. Since the modes faster than τ_α^{asPLA} account for $\sim 5\%-8\%$ of the total dielectric amplitude, we anticipate $\sim 5\%-8\%$ error in our analyses that does not affect the main conclusions.

In principle, $W(ln\tau_z)=\int_{d_0}^x \frac{dz}{d_a}$ with $d_0=d_a/2$ and $|x-d_0|=z$ due to the symmetry in the spatial gradient in segmental dynamics with respect to the middle plane at $d_0=5.3~nm$. One can then extract a spatial gradient of the relaxation time $\tau_z{\sim}z$ from $W(ln\tau_z)=\int_{-\infty}^{ln\tau_z}g(ln\tau_z)dln\tau_z$. **Figure 7b** presents the spatial gradient of the segmental relaxation

time (log-linear plot) of the three temperatures. **Figure 7c** gives the log-log plot of τ_z vs z focusing on $z=0-d_0$. Note that τ_α^{asPLA} is the fastest segmental relaxation mode in the confined amorphous polymer. We thus only keeps $\tau_z > \tau_\alpha^{asPLA}$ in our anlaysis, which leads to a gap between $z\approx 4.5-5.3$ nm for T = 353 K and T = 348 K and between z=5.0 nm -5.3 nm for T = 363 K. The main features of the spatial gradient are well captured.

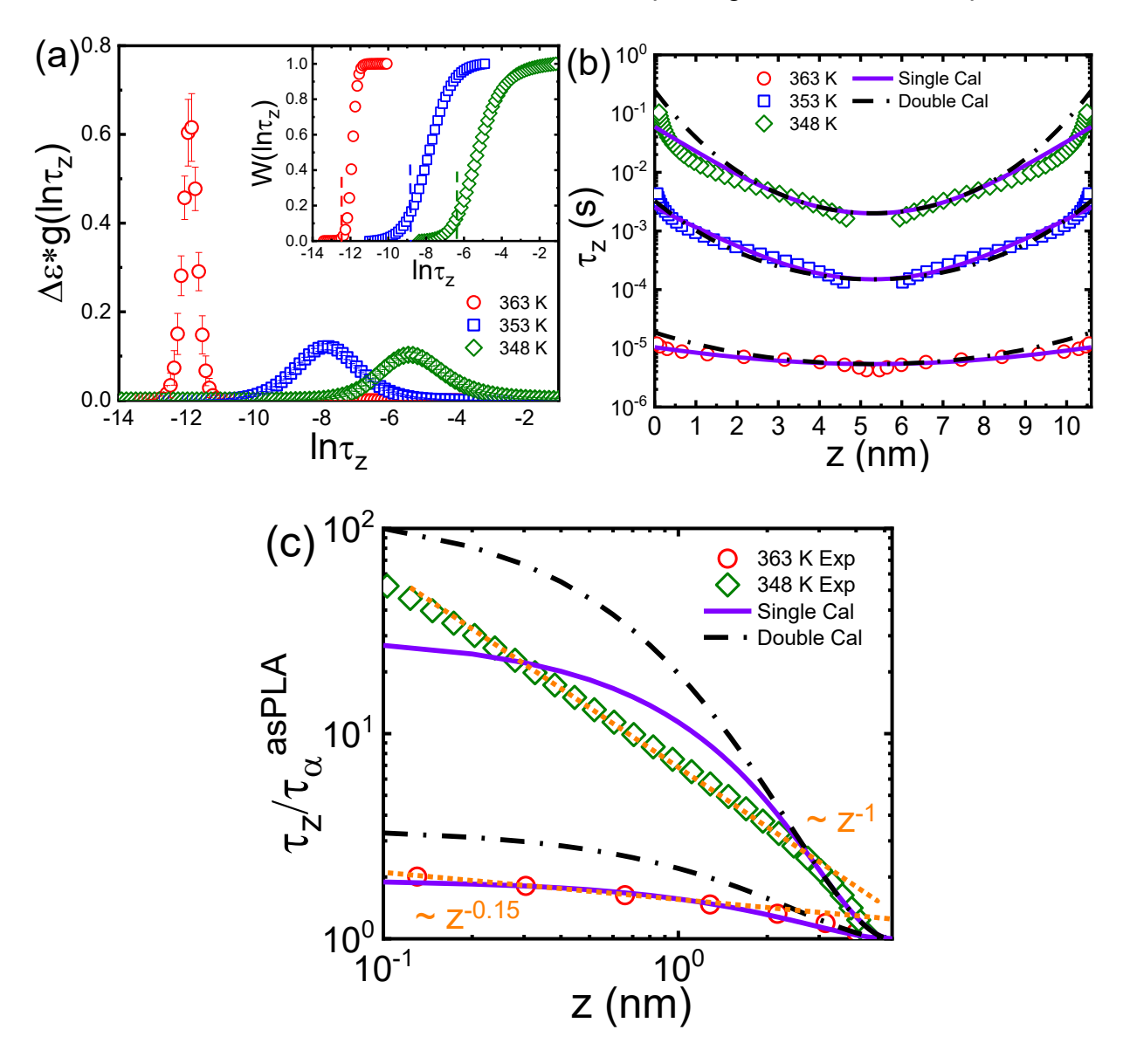


Figure 7. (a) The time distribution density function $\Delta \varepsilon * g(ln\tau_z)$ of asPLA from the relaxation time analysis at T=348~K, 353~K, and 363~K. The inset shows the accumulation of volume fractions of the dielectric contribution of polymer exhibiting relaxation time shorter than τ_z , $W(\tau_z)$. (b) The spatial gradient of relaxation time, τ_z , across the amorphous polymer phases. The x-axis, z, is the distance away from one side of the crystalline/amorphous interface. (c) The normalized spatial

gradient, $\tau_z/\tau_\alpha^{asPLA}$, in the log-log plot between z=0 - d_0 . In all panels, the symbols are from experiments. In panels (b) and (c), the solid purple lines are calculations of a single-exponential decay function suggested by random first-order transition theory. The black dash-dotted lines are calculations of a double-exponential decay function employed in a recent simulation and theoretical work (Ref. 45). The short dotted orange lines in (c) are plotted to guide eyes for a power-law relation between τ_z and z.

Table 2. Parameters to calculate the dynamics profiles in Figures 7b and 7c

T (K)	Single-exponential (Eqn.7)		Double-exponential (Eqn.8)		
	τ_s (s)	ζ (nm)	k_0	ξ (nm)	
348	5.8×10^{-2}	1.0	0.81	3.5	
353	2.5×10^{-3}	1.2	0.47	3.75	
363	8.1×10^{-6}	3.0	0.21	5.0	

3.4 Comparison between experiments and theories.

The spatial gradients provide rich information on the interface dynamics: (i) The interfacial segmental dynamics experience a sharp drop very close to the interface (1-2 nm near the interface) followed by a different decay function after that. We would like to emphasize that the total amorphous region is ~10.6 nm in thickness. Therefore, 1-2 nm at each interface accounts for ~20 – 40% of the total volume fraction of the amorphous phase. (ii) Figure 7c provides the normalized relaxation time, $\tau_z/\tau_\alpha^{asPLA}$, which shows a power law of $\tau_z/\tau_\alpha^{asPLA}\sim z^{-y}$ at z<2 nm, with y=1.0, 0.60, and 0.15 at T=348 K, T=353 K, and T=363 K respectively. Note that data of T=353 K is given in Figure 7b and not shown in Figure 7c to avoid crowdness. A smaller power law index y is observed at a higher temperature, revealing an interesting temperature dependence of the spatial gradient. The spatial gradient at z>2 nm deviates from the original power law in the double-log plot (Figure 7c).

To be more quantitative, we compare the experiments with a single exponential functional form (the purple solid lines) given by RFOT and a double exponential functional form (the black dash-dotted lines) from computer simulations at high temperatures and

the ECNLE theory. Specifically, the functional form of the single exponential dynamics gradient is⁵¹

$$\tau_z = A(z)\tau_h \quad (5)$$

where τ_b is the relaxation time of the bulk asPLA with $\tau_b = \tau_\alpha^{aPLA}$ in the current study, $A\left(z\right) \equiv \left(\frac{\tau_s}{\tau_b} - 1\right) \exp\left(-\frac{z}{\zeta}\right) + 1$, τ_s is the relaxation time right at the interface, ζ is the characteristic interfacial layer thickness that increases with cooling. On the other hand, the double-exponential decay functional form follows:^{42, 45}

$$\tau_z = (\tau_b)^{1 - \varepsilon(z)} \qquad (6)$$

where $\varepsilon(z)=k_0\exp(-\frac{z}{\xi})$ with k_0 being a prefactor and ξ a characteristic interfacial layer thickness associated with the activation energy barrier at the interface. When collective interface effect emerges, the spatial gradient of the interface dynamics becomes:

$$\tau_z = \tau_b A(z) A(H - z) \qquad (7)$$

and

$$\tau_z = (\tau_b)^{1 - (\varepsilon(z) + \varepsilon(H - z))}$$
 (8)

for the single-exponential and the double-exponential functional forms respectively. Here, $\it H$ is the gap between two neighboring interfaces. In the current study, $\it H=d_a=10.6~nm$ being the thickness of the amorphous region.

We have imposed an additional constraint: $z=d_a/2$, $\tau_z=\tau_\alpha^{asPLA}$ that leads to a one-to-one correspondence between τ_s and ζ in **Eqn. 7** and k_0 and ξ in **Eqn. 8**. **Figures 7b** and **7c** offer the calculations from the pairs of τ_s and ζ or k_0 and ξ that yield a close agreement with experiments. The purple solid lines and the black dash-dotted lines are the outcomes of the **Eqn. 7** and **Eqn. 8** at each temperature. **Table 2** summarizes the parameters associated with these calculations. In addition, the corresponding relaxation

gradients (the dashed black lines) from a single interface have also been provided in **Figure 8** to demonstrate the impact of the collective interface effect on the spatial gradient of dynamics (the symbols and the dash-dotted purple lines).

The comparison between experiments and model calculations leads to the following interesting observations: (i) Both the single exponential functional form and the double exponential functional form agree reasonably well at the regions close to the middle plane at $z = 2 - 8.6 \, nm$. (ii) The spatial gradient of dynamics close to the interface exhibits a power-law decay, which cannot be described fully by Eqn.7 or Eqn.8. (iii) Converting the relaxation time distribution back to the dielectric spectra in the frequency domain shows that neither the double-exponential functional form nor the double-exponential functional form could capture fully the strong dielectric broadening in experiments (Figure 9). These observations highlight the crucial contributions of the near interface dynamics to the dielectric spectra broadening.

At this moment, we are not sure about the physical origin leading to the deviations between the experiments and the model predictions (both the single-exponential decay functional form and the double-exponential decay functional form). One possibility could be the strong non-equilibrium chain packing of the interface as well as the potential chain orientation in the amorphous phase inherited from the pre-deformation that can affect the functional form of the spatial gradient close to the interface. Future studies with tuned interface chain conformations might be able to help clarify this issue. In addition, we free ζ and ξ in the calculations to yield the closest agreement between experiments and model calculations. This might raise additional questions of the appropriateness of such assumptions in calculations. For instance, according to the ECNLE theory and recent

computer simulations, ξ should be temperature insensitive.^{42, 45} However, we find large variations in their values from $\xi = 3.5 \ nm$ to $\xi = 5.0 \ nm$ over a small temperature range of only 15 K. On the other hand, one has to reduce ζ upon cooling in order to obtain reasonable fit to experimental data, which is opposite to the predictions of the RFOT.⁵¹ Nevertheless, the above analyses suggest a detailed characterization of the near-interface spatial gradient is promising to differentiate the fine features of different theoretical approaches.

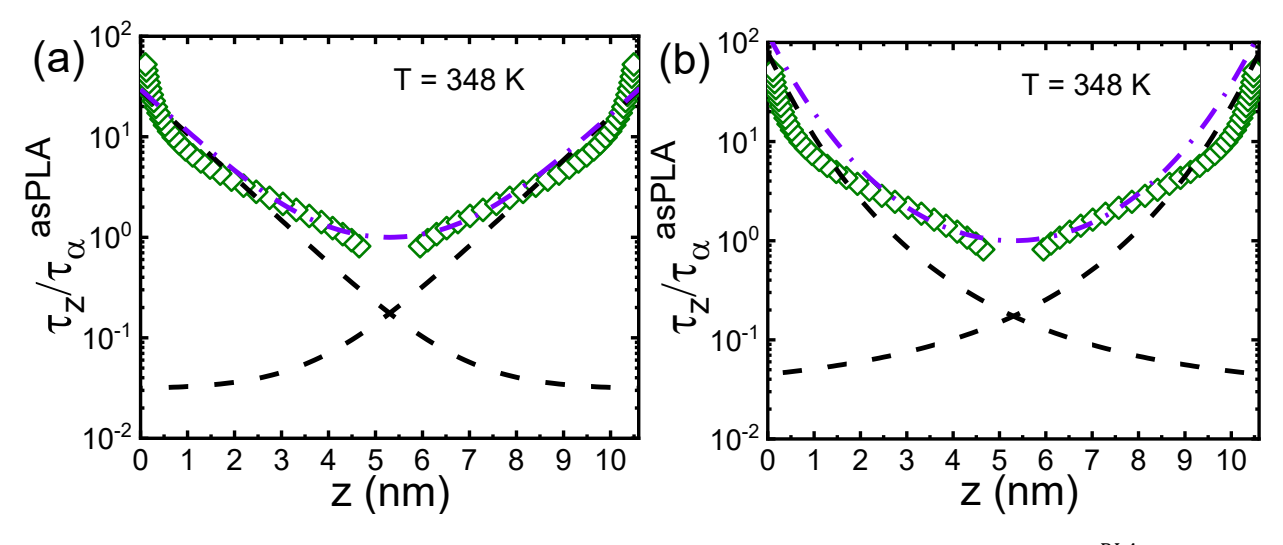


Figure 8. The comparison between experiments and the calculations of the $\tau_z/\tau_\alpha^{asPLA}$ vs z from (a) a single exponential decay function with collective interface effect (the purple dash-dotted line), and (b) a double exponential decay function with collective interface effect (the purple dash-dotted line). The dashed black lines are the corresponding calculations for a single surface in the absence of a collective interface effect in each case.

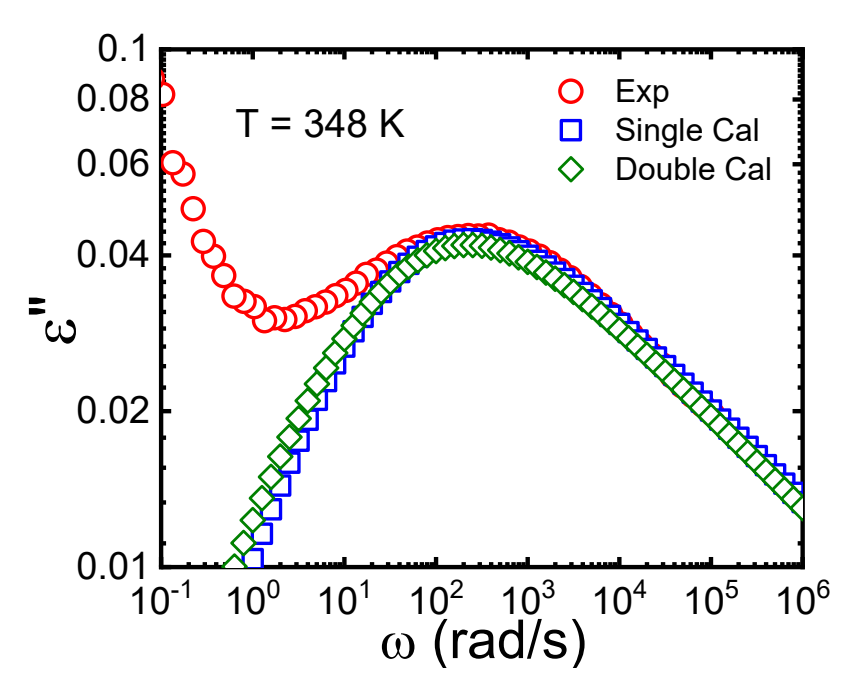


Figure 9. A comparison between the dielectric loss permittivity (the red circles) at T = 348 K and the calculated dielectric spectra using the single-exponential functional form (the blue squares, Eqn. 7) and the double exponential functional form (the olive diamonds, Eqn. 8).

3.5 Comparisons between the ILM analysis and the spatial gradient fingerprinting.

Lastly, we would like to compare the outcomes between the ILM analyses and the spatial gradient analyses. The symbols in **Figure 10** present the near-interface dynamics gradient. The dashed lines of **Figure 10** give the results of the ILM analysis, where the solid vertical line serves as the boundary between the interfacial layer and the non-interface layer polymer. The levels of the horizontal dashed lines represent τ_{α}^{int} (the large values close to the interface) or τ_{α}^{aspLA} (the smaller values away from the interface). Interestingly, the boundaries between the interfacial layer and the non-interfacial layer are all located at $\sim 1.5-2$ τ_{α}^{aspLA} for all three temperatures, which provides reasonably good representations of polymers having the fastest relaxation times. Moreover, the characteristic relaxation times of the interfacial layer, τ_{α}^{int} , from the ILM analysis intersects with the τ_z within <1 nm away from the interface (see the black arrows), representing

reasonably well the polymer dynamics close to the interface especially at high temperatures. From this perspective, the ILM analysis can indeed offer important information about the dynamic properties of polymers near the interface. We further compute the film-averaged relaxation time of the amorphous phase, $\langle \tau_z \rangle = \frac{1}{d_a} \int_0^{d_a} \tau_z dz$, which was pointed out by the arrows on the right Y-axis of the figure. This value is close to the relaxation time of at $z\approx 2\,nm$. Thus, these results indicate τ_{α}^{int} can be a much better representation of the near the interface dynamics than $\langle \tau_z \rangle$. These results also agree with the recent theoretical argument that it is challenging to distinguish different interfacial gradients from the film-averaged dynamics measurements.82 Furthermore, a closer look at au_z and au_{lpha}^{int} at different temperatures suggest a slight shift outwards from the interface at their crossover point. This implies an increase in deviations of au_{lpha}^{int} from τ_s upon cooling. These observations are consistent with an increase in the near-interface dynamics gradient upon cooling, for instance, an increase in the power index y values upon cooling shown in **Figure 7c**. One other advantage of the spatial gradient analyses is the identification of the collective interface effect, which can hardly be reflected in the ILM analysis.

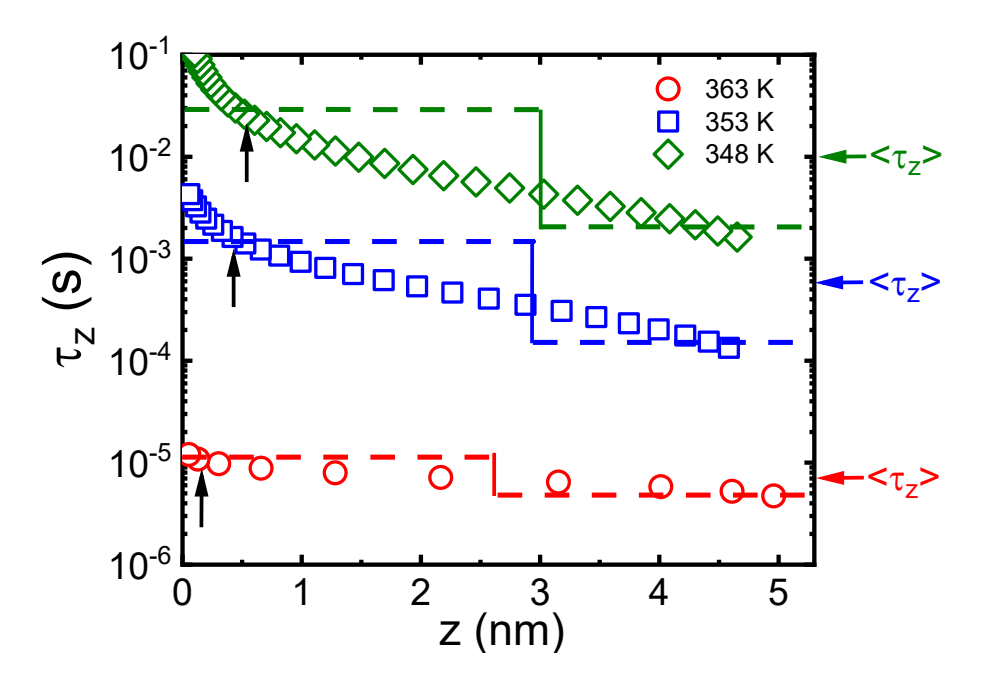


Figure 10. Comparisons of the spatial gradient fingerprinting analysis (the open symbols) and the interfacial layer model analysis (the dashed lines). The levels of the dashed lines represent the characteristic relaxation time at the polymer at the interfacial layer or the non-interfacial layer polymer. $\langle \tau_z \rangle$ is a film-averaged relaxation time of the nanoconfined amorphous PLA in asPLA.

4. Summary and Outlook

In summary, we have studied the dynamics of polymers under ultrafine nanoconfinement $\sim 10~nm$ through a new preparation of annealed semicrystalline PLA (asPLA) with controlled distributions of amorphous phases and crystalline phases. SAXS measurements suggest alternating layered structures of crystalline phases and amorphous phases of asPLA. BDS measurements show an envelope in the structural relaxation process at high temperatures. Interestingly, the dielectric dispersion envelope is slightly broader than its neat amorphous counterpart, aPLA, indicating an influence of polymer processing on the local molecular packing of the asPLA. Moreover, strong asymmetric dielectric broadening at the low frequencies has been observed for asPLA upon cooling, highlighting the presence of amorphous/crystalline interface to polymer dynamics. The asPLA also exhibits a large increase in T_g and a strong increment in the

fragility index m with respect to aPLA, revealing the large influence of the ultrafine nanoconfinement and a collective interface effect.

We have employed a phenomenological interfacial layer model (ILM) and have developed a new analysis to quantify the spatial gradient of the near-interface dynamics. The ILM model provides average interfacial polymer dynamics, the thickness of the interfacial layer, and the dynamics of the non-interfacial polymer. On the other hand, the spatial gradient fingerprinting method reveals fine features of the relaxation time profile across the amorphous phase. Interestingly, comparisons between the experimental spatial gradient of dynamics with the theoretical predictions have demonstrated reasonable agreement at high temperatures. However, obvious deviations were found at low temperatures from either a single-exponential decay functional form suggested by RFOT or a double-exponential decay functional form from the ECNLE theory. The origin of these deviations is not clear at this moment and might be related to the non-equilibrium packing of the polymer at the crystalline/amorphous interface.

Lastly, we would like to emphasize that although the current study focuses on only one semi-crystalline polymer with one pre-deformation condition, *i.e.*, an elongation ratio $\lambda=4.0$, which leads to one nanoconfinement condition of a film thickness of 10.6~nm. The sample preparation methods can be extended to many other semi-crystalline polymers as demonstrated in recent works. Furthermore, the proposed spatial gradient analyses through dielectric measurements are not polymer-specific. Therefore, we anticipate the analyses discussed in this study to be applicable to other nanoconfined systems, such as polymer nanocomposites, block copolymers, polymer thin films, polymers infiltrated into nanopores, etc.

Supplementary Material

The supplementary Material contains additional data and analysis to support the main context, including (i) Linear viscoelastic measurements of sPLA at high temperatures; (ii) Differential Scanning Calorimetry measurements to quantify the cold recrystallization temperature of sPLA; (iii) Dielectric measeurements to demonstrate the negligible changes of dielectric function upon heating and cooling; (iv) Wide angle x-ray diffraction for the crystalline form of asPLA; (v) Additional analysis of the Differential Scanning Calorimetry measurements; (vi) Additional analysis of the dielectric spectra of the asPLA and aPLA.

Acknowledgment

This work was supported by the National Science Foundation with the Award Number NSF-DMR 2211573. This material is based upon work supported by the U.S. Department of Energy's Office of Energy Efficiency and Renewable Energy (EERE) under the Advanced Manufacturing Technology Office, Award Number DE-EE0009947. The authors thank Prof. Qiang Zhe's group at the University of Southern Mississippi for help on the SEC measurements for molecular weight and molecular weight distribution. The authors thank Prof. Liheng Cai's group at the University of Virginia for help on the small angle x-ray scattering measurements. This research used the SMI beamline (12-ID) of the National Synchrotron Light Source II, a U.S. Department of Energy (DOE) Office of Science User Facility operated for the DOE Office of Science by Brookhaven National Laboratory under contract no. DE-SC0012704. We thank Prof. Shiyou Ding's group at MSU to help us on the Atomic Force Microscopy measurements.

Author Declarations

Conflicts of Interest

The authors have no conflicts to disclose.

Data Availability

All relevant data are included in the paper and in the supplementary materials (SM). Raw experimental data and analyses are available upon reasonable request from S.C.

Reference

- ¹ M. D. Ediger, and J. A. Forrest, Macromolecules **47** (2014) 471.
- ² J. Baschnagel, and F. Varnik, J. Phys. Condens. Matter **17** (2005) R851.
- ³B. A. Pazmino Betancourt, J. F. Douglas, and F. W. Starr, Soft Matter **9** (2013) 241.
- ⁴D. S. Simmons, Macromol. Chem. Phys. **217** (2016) 137.
- ⁵ N. Simone, G. Emmanouil, and B. T. Nicholas, Rep. Prog. Phys. **80** (2017) 036602.
- ⁶ R. D. Priestley, C. J. Ellison, L. J. Broadbelt, and J. M. Torkelson, Science **309** (2005) 456.
- ⁷Y. Chai, T. Salez, J. D. McGraw, M. Benzaquen, K. Dalnoki-Veress, E. Raphaël, and J. A. Forrest, Science **343** (2014) 994.
- ⁸ Z. Fakhraai, and J. A. Forrest, Science **319** (2008) 600.
- ⁹ S. E. Harton, S. K. Kumar, H. Yang, T. Koga, K. Hicks, E. Lee, J. Mijovic, M. Liu, R. S. Vallery, and D. W. Gidley, Macromolecules **43** (2010) 3415.
- ¹⁰ T. Koga, N. Jiang, P. Gin, M. K. Endoh, S. Narayanan, L. B. Lurio, and S. K. Sinha, Phys. Rev. Lett. **107** (2011) 225901.
- ¹¹ P. Gin, N. Jiang, C. Liang, T. Taniguchi, B. Akgun, S. K. Satija, M. K. Endoh, and T. Koga, Phys. Rev. Lett. **109** (2012) 265501.
- ¹² N. Jiang, J. Shang, X. Di, M. K. Endoh, and T. Koga, Macromolecules **47** (2014) 2682. ¹³ N. Jiang, M. K. Endoh, and T. Koga, in *Non-equilibrium Phenomena in Confined Soft Matter: Irreversible Adsorption, Physical Aging and Glass Transition at the Nanoscale*, edited by S. Napolitano (Springer International Publishing, Cham, 2015), pp. 129.
- ¹⁴ N. Jiang, M. K. Endoh, T. Koga, T. Masui, H. Kishimoto, M. Nagao, S. K. Satija, and T. Taniguchi, ACS Macro Letters (2015) 838.
- ¹⁵ M. Sen, N. Jiang, J. Cheung, M. K. Endoh, T. Koga, D. Kawaguchi, and K. Tanaka, ACS Macro Letters (2016) 504.
- ¹⁶ D. A. Barkley, N. Jiang, M. Sen, M. K. Endoh, J. G. Rudick, T. Koga, Y. Zhang, O. Gang, G. Yuan, S. K. Satija, D. Kawaguchi, K. Tanaka, and A. Karim, Macromolecules **50** (2017) 7657.
- ¹⁷ T. Koga, D. Barkley, M. Nagao, T. Taniguchi, J.-M. Y. Carrillo, B. G. Sumpter, T. Masui, H. Kishimoto, M. Koga, J. G. Rudick, and M. K. Endoh, Macromolecules **51** (2018) 9462.

- ¹⁸ R. L. Jones, S. K. Kumar, D. L. Ho, R. M. Briber, and T. P. Russell, Nature **400** (1999) 146.
- ¹⁹ R. L. Jones, S. K. Kumar, D. L. Ho, R. M. Briber, and T. P. Russell, Macromolecules 34 (2001) 559. ²⁰ B. Wunderlich, Prog. Polym. Sci. **28** (2003) 383.
- ²¹ J. Lee, J. H. Mangalara, and D. S. Simmons, J. Polym. Sci., Part B: Polym. Phys. **55** (2017)907.
- ²² M. Z. Slimani, A. J. Moreno, G. Rossi, and J. Colmenero, Macromolecules **46** (2013) 5066.
- ²³ C. B. Roth, and J. M. Torkelson, Macromolecules **40** (2007) 3328.
- ²⁴ D. Christie, R. A. Register, and R. D. Priestley, ACS Central Science **4** (2018) 504.
- ²⁵ I. Popov, S. Cheng, and A. P. Sokolov, in *Macromolecular Engineering*, edited by K. Matyjaszewski, Y. Gnanou, N. Hadjichristidis, and M. Muthukumar2022), pp. 1.
- ²⁶ S. Cheng, in *Dynamics of Composite Materials*, edited by A. Schönhals, and P. Szymoniak (Springer International Publishing, Cham, 2022), pp. 63.
- ²⁷ S. Cheng, in *Broadband Dielectric Spectroscopy: A Modern Analytical Technique* (American Chemical Society, 2021), pp. 157. ²⁸ S. Cheng, S.-J. Xie, J.-M. Y. Carrillo, B. Carroll, H. Martin, P.-F. Cao, M. D. Dadmun,
- B. G. Sumpter, V. N. Novikov, K. S. Schweizer, and A. P. Sokolov, ACS Nano 11 (2017) 752.
- ²⁹ S. Cheng, B. Carroll, V. Bocharova, J.-M. Carrillo, B. G. Sumpter, and A. P. Sokolov, J. Chem. Phys. 146 (2017) 203201.
- ³⁰ E. J. Bailey, and K. I. Winey, Prog. Polym. Sci. (2020) 101242.
- ³¹ C.-H. Tu, J. Zhou, H.-J. Butt, and G. Floudas, Macromolecules **54** (2021) 6267.
- ³² C.-H. Tu, J. Zhou, M. Doi, H.-J. Butt, and G. Floudas, Phys. Rev. Lett. **125** (2020) 127802.
- ³³ I. Popov, B. Carroll, V. Bocharova, A.-C. Genix, S. Cheng, A. Khamzin, A. Kisliuk, and A. P. Sokolov, Macromolecules 53 (2020) 4126.
- ³⁴ S. Cheng, and A. P. Sokolov, J. Chem. Phys. **152** (2020) 094904.
- 35 S. Cheng, B. Carroll, W. Lu, F. Fan, J.-M. Y. Carrillo, H. Martin, A. P. Holt, N.-G. Kang, V. Bocharova, J. W. Mays, B. G. Sumpter, M. Dadmun, and A. P. Sokolov, Macromolecules 50 (2017) 2397.
- ³⁶ B. Carroll, S. Cheng, and A. P. Sokolov, Macromolecules **50** (2017) 6149.
- ³⁷ A. P. Holt, V. Bocharova, S. Cheng, A. M. Kisliuk, B. T. White, T. Saito, D. Uhrig, J. P. Mahalik, R. Kumar, A. E. Imel, T. Etampawala, H. Martin, N. Sikes, B. G. Sumpter, M. D. Dadmun, and A. P. Sokolov, ACS Nano 10 (2016) 6843.
- ³⁸ S. Cheng, A. P. Holt, H. Wang, F. Fan, V. Bocharova, H. Martin, T. Etampawala, B. T. White, T. Saito, N.-G. Kang, M. D. Dadmun, J. W. Mays, and A. P. Sokolov, Phys. Rev. Lett. **116** (2016) 038302.
- ³⁹ S. Cheng, S. Mirigian, J.-M. Y. Carrillo, V. Bocharova, B. G. Sumpter, K. S. Schweizer, and A. P. Sokolov, J. Chem. Phys. 143 (2015) 194704.
- ⁴⁰ A. Papon, H. Montes, M. Hanafi, F. Lequeux, L. Guy, and K. Saalwächter, Phys. Rev. Lett. 108 (2012) 065702.
- ⁴¹ B. D. Vogt, J. Polym. Sci., Part B: Polym. Phys. **56** (2018) 9.
- ⁴² A. Ghanekarade, A. D. Phan, K. S. Schweizer, and D. S. Simmons, Nat. Phys. **19** (2023) 800.

- ⁴³ T. Rahman, and D. S. Simmons, Macromolecules **54** (2021) 5935.
- ⁴⁴ Z. Hao, A. Ghanekarade, N. Zhu, K. Randazzo, D. Kawaguchi, K. Tanaka, X. Wang, D. S. Simmons, R. D. Priestley, and B. Zuo, Nature **596** (2021) 372.
- ⁴⁵ A. Ghanekarade, A. D. Phan, K. S. Schweizer, and D. S. Simmons, Proc. Nat. Acad. Sci. U.S.A. **118** (2021) e2104398118.
- ⁴⁶ R. J. Lang, and D. S. Simmons, Macromolecules **46** (2013) 9818.
- ⁴⁷ P. Z. Hanakata, J. F. Douglas, and F. W. Starr, Nat Commun **5** (2014) 4163.
- ⁴⁸ F. W. Starr, and J. F. Douglas, Phys. Rev. Lett. **106** (2011) 115702.
- ⁴⁹ P. Scheidler, W. Kob, and K. Binder, J. Phys. Chem. B **108** (2004) 6673.
- ⁵⁰ J.-M. Y. Carrillo, S. Cheng, R. Kumar, M. Goswami, A. P. Sokolov, and B. G. Sumpter, Macromolecules **48** (2015) 4207.
- ⁵¹ J. D. Stevenson, and P. G. Wolynes, J. Chem. Phys. **129** (2008) 234514.
- ⁵² K. S. Schweizer, and D. S. Simmons, J. Chem. Phys. **151** (2019) 240901.
- ⁵³ R. P. White, and J. E. G. Lipson, Phys. Rev. Lett. **131** (2023) 018101.
- ⁵⁴ R. P. White, C. C. Price, and J. E. G. Lipson, Macromolecules **48** (2015) 4132.
- ⁵⁵ A. D. Phan, and K. S. Schweizer, ACS Macro Letters (2020) 448.
- ⁵⁶ V. V. Ginzburg, Macromolecules **55** (2022) 873.
- ⁵⁷ W. Zhang, F. W. Starr, and J. F. Douglas, J. Chem. Phys. **155** (2021) 174901.
- ⁵⁸ D. Diaz-Vela, J.-H. Hung, and D. S. Simmons, ACS Macro Letters **7** (2018) 1295.
- ⁵⁹ A. D. Phan, and K. S. Schweizer, J. Chem. Phys. **150** (2019) 044508.
- ⁶⁰ A. D. Phan, and K. S. Schweizer, Macromolecules **51** (2018) 6063.
- ⁶¹ S. Alexandris, G. Sakellariou, M. Steinhart, and G. Floudas, Macromolecules **47** (2014) 3895.
- ⁶² S. Napolitano, S. Capponi, and B. Vanroy, Eur Phys J E **36**, 61 (2013) 61.
- ⁶³ M. Tress, M. Erber, E. U. Mapesa, H. Huth, J. Müller, A. Serghei, C. Schick, K.-J. Eichhorn, B. Voit, and F. Kremer, Macromolecules **43** (2010) 9937.
- ⁶⁴ A. Serghei, M. Tress, and F. Kremer, J. Chem. Phys. **131** (2009) 154904.
- ⁶⁵ M. Tress, E. U. Mapesa, W. Kossack, W. K. Kipnusu, M. Reiche, and F. Kremer, Science **341** (2013) 1371.
- ⁶⁶ F. Kremer, E. U. Mapesa, M. Tress, and M. Reiche, in *Recent Advances in Broadband Dielectric Spectroscopy*, edited by Y. P. Kalmykov (Springer Netherlands, 2013), pp. 163.
- ⁶⁷ T. Smith, J. Feng, L. Zou, M. Gao, M. Prévôt, and S.-Q. Wang, Macromol. Rapid Commun. **44** (2023) 2200293.
- ⁶⁸ M. Razavi, W. Zhang, H. A. Khonakdar, A. Janke, L. Li, and S.-Q. Wang, Soft Matter **17** (2021) 1457.
- ⁶⁹ M. Razavi, and S.-Q. Wang, Macromolecules **52** (2019) 5429.
- ⁷⁰ S. Cheng, Y. Lu, G. Liu, and S.-Q. Wang, Soft Matter **12** (2016) 3340.
- ⁷¹ M. C. Righetti, M. Gazzano, M. L. Di Lorenzo, and R. Androsch, Eur. Polym. J. **70** (2015) 215.
- ⁷² M. Pyda, R. C. Bopp, and B. Wunderlich, The Journal of Chemical Thermodynamics **36** (2004) 731.
- ⁷³ M. Pyda, and A. Czerniecka-Kubicka, in *Synthesis, Structure and Properties of Poly(lactic acid)*, edited by M. L. Di Lorenzo, and R. Androsch (Springer International Publishing, Cham, 2018), pp. 153.
- ⁷⁴ Z. Wang, M. Schaller, A. Petzold, K. Saalwächter, and T. Thurn-Albrecht, Proc. Nat. Acad. Sci. U.S.A. **120** (2023) e2217363120.

- ⁷⁵ G. Strobl, *The Physics of Polymers* (Springer Berlin, Heidelberg, Berlin Heidelberg, 2007), 484-491.
- ⁷⁶ W. Guo, B. Yang, R. Xia, L. Su, J. Miao, J. Qian, P. Chen, X. Yu, Q. Zhang, and S. Deng, Journal of Research Updates in Polymer Science **2** (2013) 168.
- ⁷⁷ C. Dalle-Ferrier, A. Kisliuk, L. Hong, G. CariniJr., G. Carini, G. D'Angelo, C. Alba-Simionesco, V. N. Novikov, and A. P. Sokolov, J. Chem. Phys. **145** (2016) 154901.
- ⁷⁸ A. P. Sokolov, V. N. Novikov, and Y. Ding, J. Phys. Condens. Matter **19** (2007) 205116. ⁷⁹ H. Emamy, S. K. Kumar, and F. W. Starr, Phys. Rev. Lett. **121** (2018) 207801.
- ⁸⁰ T. Roths, M. Marth, J. Weese, and J. Honerkamp, Comput. Phys. Commun. **139** (2001) 279.
- ⁸¹ F. Kremer, and A. Schohals, *Broadband Dielectric Spectroscopy* (Springer-Verlag, Berlin, 2002),
- 82 D. Diaz Vela, A. Ghanekarade, and D. S. Simmons, Macromolecules 53 (2020) 4158.